Journal of Materials Chemistry C

RSC Publishing

PAPER

View Article Online
View Journal | View Issue

Cite this: J. Mater. Chem. C, 2013, 1, 3017

Synergic effect within n-type inorganic–p-type organic nano-hybrids in gas sensors†

Tingting Jiang,‡[a] Zhaojie Wang,‡[a] Zhenyu Li,*[ab] Wei Wang,[a] Xiuru Xu,[a] Xincai Liu,[a] Jinfeng Wang[b] and Ce Wang*[a]

Received 9th October 2012
Accepted 7th March 2013

DOI: 10.1039/c3tc00370a

www.rsc.org/MaterialsC

This paper describes the exploration of a synergic effect within n-type inorganic–p-type organic nano-hybrids in gas sensors. One-dimensional (1D) n-type SnO_2–p-type PPy composite nanofibers were prepared by combining the electrospinning and polymerization techniques, and taken as models to explore the synergic effect during the sensing measurement. Outstanding sensing performances, such as large responses and low detection limits (20 ppb for ammonia) were obtained. A plausible mechanism for the synergic effect was established by introducing p–n junction theory to the systems. Moreover, interfacial metal (Ag) nanoparticles were introduced into the n-type SnO_2–p-type PPy nano-hybrids to further supplement and verify our theory. The generality of this mechanism was further verified using TiO_2–PPy and TiO_2–Au–PPy nano-hybrids. We believe that our results can construct a powerful platform to better understand the relationship between the microstructures and their gas sensing performances.

1 Introduction

The past several decades have witnessed huge progress in fabricating diverse functional micro(nano)-devices, such as transistors,[1–3] solar cells,[4–8] photovoltaic devices,[9,10] memory elements,[11–13] diode devices,[14–18] thermosensitive devices,[19,20] pH-sensors,[21] luminescence devices[22] and light-emitting electrochemical cells (LECs),[23] based on inorganic–organic nano-hybrids driven by the unique synergic effect between n-type inorganic and p-type organic structural hybrid materials within single components. Among those functional devices, gas sensors have been given special attention owing to their practical applications in environmental monitoring, industrial process control, and our daily life. Before now, many sensitive gas sensors were successfully obtained based on inorganic–organic nano-hybrids.[24–28] For example, Kimura *et al.* reported that TiO_2 porous films coated with polythiophene layers worked as highly sensitive sensing interfaces, which can output two signals for weight and resistance changes upon exposure to VOC vapor.[29] Ammam and Easton prepared novel inorganic–organic hybrid semiconducting nanomaterials formed between pyrrole and Dawson type polyoxoanions, which exhibited interesting extended linearity up to 5500 ppm NO_x.[30] Gold nanoparticles stabilised with short ω-functionalised ligands were fabricated by Evans *et al.*, which were sensitive to different analytes and displayed different conductometric and ellipsometric responses depending on the nature of the ω-functional group.[31] Pinto *et al.*, reported inorganic–organic hybrid semiconductor Schottky nanodiodes by electrospinning polyaniline nanofibers and an inorganic n-doped semiconductor, making them attractive candidates for low power, supersensitive, and rapid response sensors as well.[32]

Recently, 1D continuous inorganic–organic nano-hybrids have been widely investigated in the sensing field due to their high surface to volume ratios, and special physical and chemical properties.[33–45] Although many successes have been achieved, the synergic effect between the n-type semiconductors and p-type conducting polymer and its role in gas sensing behavior is still not clear. Therefore, here we design and carry out a series of rational experiments to clarify the synergic effect in n-type inorganic–p-type organic nano-hybrids during gas sensing measurements.

In this paper, 1D n-type SnO_2–p-type PPy hybrid nanofibers are prepared through electrospinning followed by *in situ* vapor phase polymerization, and used as models to explore the synergic effect between inorganic and organic nano-hybrids. A large response and low detection limit (20 ppb) were achieved during the gas sensing measurement. p–n junction theory has been used to explain the synergic effect in gas sensing measurements for NH_3. Furthermore, 1D TiO_2–PPy and TiO_2–Au–PPy nano-hybrid-structures have also been fabricated to supplement and verify the generality of our theory. Outstanding sensing performances have been also achieved. Most importantly, we believe that our results can construct a powerful

[a]Alan G. MacDiarmid Institute, Jilin University, Changchun 130012, P. R. China. E-mail: zhenyu_li@jlu.edu.cn; zhenyuli@deakin.edu.au; cwang@jlu.edu.cn; Fax: +86 431 85168292; Tel: +86 431 85168292

[b]Australian Future Fibres Research & Innovation Centre, Institute for Frontier materials, Deakin University, Geelong, Victoria 3217, Australia

† Electronic supplementary information (ESI) available: Materials and methods for syntheses and experiments. See DOI: 10.1039/c3tc00370a

‡ These authors contributed equally to this work.

platform to better understand the relationship between the microstructures and their gas sensing performances.

2 Experimental

2.1 Chemicals

Ethanol (>95%) and *N*, *N*-dimethyl formamide (>95%) were purchased from Tianjin Chemical Company. Poly (vinyl pyrrolidone) (PVP, M_w = 1 300 000), $SnCl_2 \cdot 2H_2O$, and $FeCl_3 \cdot 9H_2O$ were purchased from Aldrich. Pyrrole was purchased from Sinopharm Chemical Reagent Co., Ltd. All chemicals were used as received without any further purification.

2.2 Preparation and characterization of PPy-coated nanofibers

In a typical procedure, equimolar $SnCl_2 \cdot 2H_2O$ and $FeCl_3 \cdot 9H_2O$ were dissolved in 1 : 1 weight ratio of DMF and ethanol mixture under vigorous stirring for 30 min. Subsequently, 0.8 g of poly(vinyl pyrrolidone) (PVP) was added to this solution under vigorous stirring for 6 h. Then, the mixture was loaded into a glass syringe with a pinhead internal diameter of 0.8 mm. The pinhead was connected to a high voltage supply that was capable of generating direct current (DC) voltages of up to 30 kV. In our experiment, a voltage of 12 kV was applied for electrospinning. An aluminum foil served as the counter electrode, and the distance between the capillary and the substrate electrode was 20 cm. The as-spun nanofibers collected on the flat aluminum foil were transferred to a crucible and the complete removal of PVP was achieved by calcinating at 600 °C for 4 h in air. The ceramic nanofibers were exposed to HCl and saturated pyrrole vapor in turn under ambient conditions in a vacuum drier at room temperature.

Ag nanoparticles were deposited on the surface of Fe_2O_3–SnO_2 nanofibers by dipping the nanofibers into diluted $AgNO_3$ solution and then reducing under UV irradiation. PPy–TiO_2 core–shell nanofibers were fabricated according to ref. 62, while PPy–Au–TiO_2 core–shell nanofibers were prepared by adding 5 at.% $HAuCl_4 \cdot 6H_2O$ during electrospinning of the TiO_2 nanofibers. The experimental details can be found in the ESI.†

The fibrous mat was characterized using transmission electron micrographs (TEM, JEX-1200EX microscope), energy dispersive X-ray (EDX) spectroscopy (SSX-550, Shimadzu), X-ray diffraction (XRD, Siemens D5005 diffractometer using Cu Kα radiation).

Fourier transform infrared (FT-IR) spectra of KBr powder-pressed pellets were recorded on a BRUKER VECTOR22 Spectrometer. Thermal gravimetric analysis (TGA) was employed to evaluate the weight loss of the samples in air at a heating rate of 5 °C min^{-1} through a thermal analyzer (Perkin-Elmer PYRIS 1).

2.3 *I–V* measurement

A pair of 100 nm thick gold electrodes with a 60 μm channel spacing was first evaporated onto the SiO_2 wafer. The as-prepared nanofibers (2 mg) were dissolved in 200 μL of distilled water. After ultrasonication (2 min), uniformly dispersed nanofibers were obtained. Then 10 μL of nanofiber solution (namely, 0.1 mg of the sample) was dipped onto the channel spacing and the electrodes were dried in shade. The *I–V* curves of these devices were measured by a Keithley 2400.

2.4 Preparation of the sensor device

The as-prepared coated composite nanofibers were ground and mixed with deionized water in a weight ratio of 100 : 25 to form a dilute paste. The paste was screen-printed onto a ceramic substrate (10 mm × 5 mm, 0.5 mm thick) with three pairs of carbon interdigital electrodes (electrode width and distance: 0.15 mm) to form a film with a thickness of around 10 μm, and then the film was dried in the shade for one day.

Gas sensing properties were measured using a static test system. The electrical properties of the sensors were measured by the CGS-8 intelligent gas-sensing analysis system (Beijing Elite Tech Co. Ltd., China). The source of the voltage used in the system was AC 220 V and the sensor test voltage supplied by the system was DC 5 V. When the resistances of all the sensors were stable, saturated target gas was injected into the test chamber (20 L in volume) by a microsyringe through a rubber plug. The saturated target gas was mixed with air (relative humidity was about 40% and room temperature was about 25 °C) by two fans in the analysis system. After the sensor resistances reached a new constant value, the test chamber was opened to recover the sensors in air. All the measurements were performed in a laboratory fume hood. The sensor resistance and response values were acquired by the analysis system automatically.

3 Results and discussion

3.1 1D SnO_2–Fe_2O_3 composite nanofibers

Fig. 1a shows a typical TEM image of as-prepared SnO_2–Fe_2O_3 composite nanofibers, indicating that the average diameter is 52 ± 3 nm. Additionally, some pores can be observed on the SnO_2–Fe_2O_3 composite nanofibers, which are caused by the decomposition of PVP during the process of calcination.[46] The samples appear brownish yellow (inset in Fig. 1a). Fig. 1b displays the XRD patterns of the composite nanofibers. Clear peaks at 2θ = 26.6°, 33.9°, 37.9°, 51.8°, 54.7°, 57.9°, 61.9°, 64.7°, 65.9°, 71.3° and 78.8° correspond to the (110), (101), (200), (211), (220), (002), (310), (112), (301), (202) and (321) crystal planes of tetragonal rutile SnO_2 (JCPDS 41-1445). Additionally, six peaks at 2θ = 24.2°, 33.2°, 35.7°, 39.4°, 40.9° and 49.6° corresponding

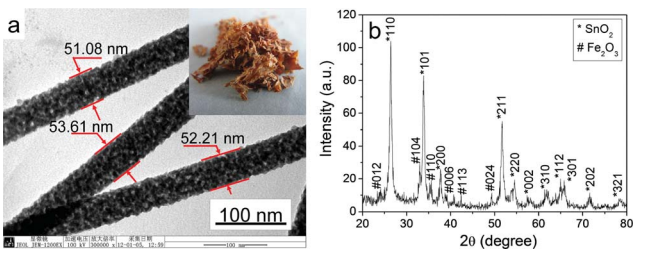

Fig. 1 (a) TEM image and (b) XRD pattern of the SnO_2–Fe_2O_3 composite nanofibers.

to the (012), (104), (110), (006), (113) and (024) crystal planes of hexagonal α-Fe_2O_3 (JCPDS 84-0307) can be also detected.

3.2 Synthesis of 1D SnO_2–PPy composite nanofibers *via* vapor phase polymerization

To fabricate 1D SnO_2–PPy composite nanofibers, SnO_2–Fe_2O_3 composite nanofibers were used as a template by exposure to HCl and saturated pyrrole vapor in turn under ambient conditions in a vacuum drier at room temperature (25 ± 1 °C). During this process, Fe_2O_3 reacted with HCl vapor to form $FeCl_3$. Then $FeCl_3$ acted as the oxidant to polymerize the PPy layer on the surface of the SnO_2 nanofibers.[47,48] To track this reaction, XRD (as shown in Fig. 2) has been used to characterize the SnO_2–PPy composite nanofibers with different PPy layer thicknesses. Four samples with different PPy layer thicknesses, namely SnO_2–PPy-0.5 h, SnO_2–PPy-1 h, SnO_2–PPy-2 h, and SnO_2–PPy-3 h were prepared with vapor phase polymerization times of 0.5, 1, 2, and 3 h, respectively. Peaks of hexagonal α-Fe_2O_3 disappeared in the XRD after exposure to HCl, confirming the interaction between Fe_2O_3 and HCl vapor. Meanwhile, peaks of the tetragonal rutile SnO_2 became broader owing to the coated PPy nanolayer blocking the contact between SnO_2 grains. Fig. 3 presents the TEM images of the SnO_2–PPy composite nanofibers. When the polymerization time was less than or equal to 1 h, the PPy coating was not clearly observed from the TEM images (as shown in Fig. 3a and b) for the low speed of vapor phase polymerization. However the color of the composite fibers changed from brownish yellow to black (inset in Fig. 3a and b), confirming the formation of the PPy layer on the surface of the SnO_2 nanofibers. When the polymerization time was 2 h, a thin PPy layer with an average thickness of 23 ± 4 nm could be clearly observed on the surface of the SnO_2 nanofibers (Fig. 3c). When the polymerization time was prolonged from 2 h to 3 h, the PPy layer thickness increased from 23 ± 4 nm to 30 ± 2 nm (Fig. 3d).

To further prove the formation of a PPy nanolayer during the polymerization process, both FT-IR and TGA were used to characterize the samples. Fig. 4a shows the FT-IR spectra of the samples, in which two typical characteristic peaks at 1550 and 1463 cm^{-1}, corresponding to typical polypyrrole ring vibrations, can be observed. Additionally, the bands at 1309 and 1049 cm^{-1} were assigned to the =C–H in plane vibration. The broad band at 1186 cm^{-1} was assigned to N–C stretching. The peak observed at 883 cm^{-1} was assigned to the =C–H out of plane vibration indicating the polymerization of pyrrole.[39] The PPy content within the samples was measured by TGA as shown in Fig. 4b. From the curves, it can be found that the weight loss (wt%), caused by the decomposition of PPy, increased gradually as the polymerization time was prolonged, confirming that the PPy contents within the samples were ~10 wt%, 15 wt%, 18 wt%, and 20 wt%, for polymerization times of 0.5, 1, 2 and 3 h, respectively.

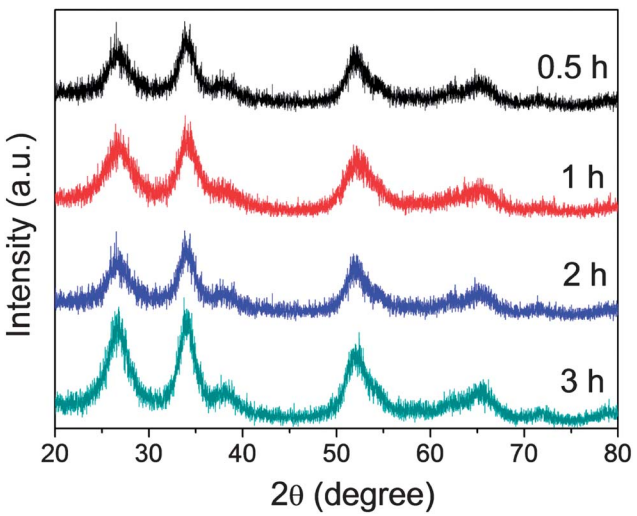

Fig. 2 XRD patterns of SnO_2–PPy hybrid nanofibers with different polymerization times from 0.5 h to 3 h.

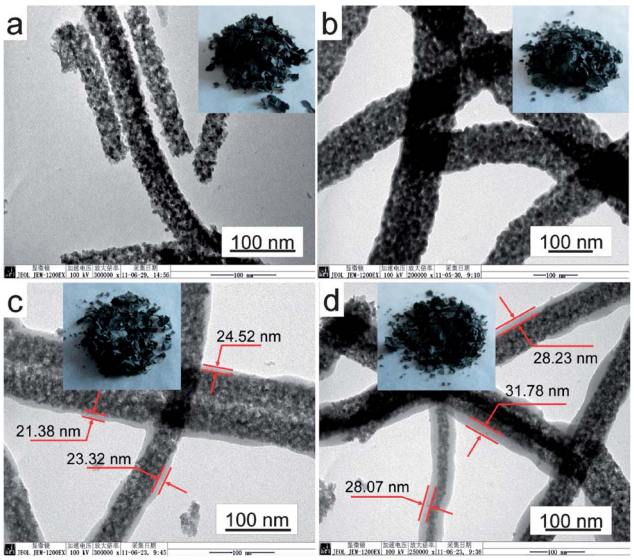

Fig. 3 TEM images of SnO_2–PPy hybrid nanofibers with different polymerization times: (a) 0.5 h, (b) 1 h, (c) 2 h, (d) 3 h. The insets show the optical photographs.

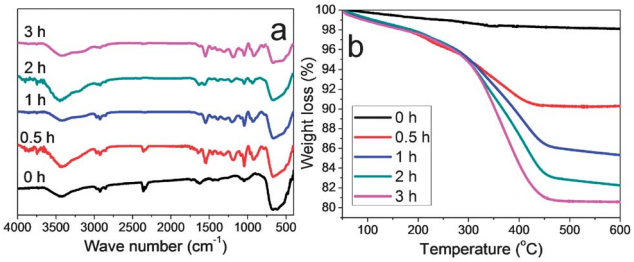

Fig. 4 (a) FT-IR spectra and (b) thermal analysis results of SnO_2–PPy hybrid nanofibers with different polymerization times.

3.3 Gas sensing performances based on 1D SnO_2–PPy composite nanofibers and the interactions between PPy and NH_3

In our experiments, the response (S) is defined as $S = \frac{R_g - R_a}{R_a} \times 100\,(\%)$, in which R_a is the resistance of the device in air and R_g is the resistance in a certain concentration of NH_3.

Fig. 5 shows that the response changes as the NH_3 concentration changes (20 ppb to 500 ppm). Among the samples, SnO_2–PPy-1 h shows the largest response. The response value of SnO_2–PPy is higher than 3% at 20 ppb of NH_3 (as shown in Fig. S1†), which surpasses most of the existing gas devices based on PPy–inorganic nano-hybrid-structures.[26,49–53] The responses of all the samples increases rapidly as the NH_3 concentration is increased and remain unsaturated at 500 ppm of NH_3, displaying a very wide detection range. As shown in the inset of Fig. 5, the response presents good linearity with the concentration of NH_3 when the concentration of NH_3 is lower than 1000 ppb.

Fig. 6 shows typical electrical responses of the four devices as a function of time upon periodic exposure to 20, 100 and 500 ppm of NH_3, respectively. Air was chosen as the carrier gas in the experiments in order to simulate the most common sensing environment. From Fig. 6, it can be clearly seen that the resistance of PPy-coated nanofibers increases rapidly upon exposure to NH_3 and then gradually levels off. The response shows a concentration-dependent behavior. By purging with air, the sensor response can be recovered quickly. Moreover, the response at high concentration is much faster than that at low concentration. This observation is in good agreement with previous reports of PPy-based NH_3 sensors.[54,55]

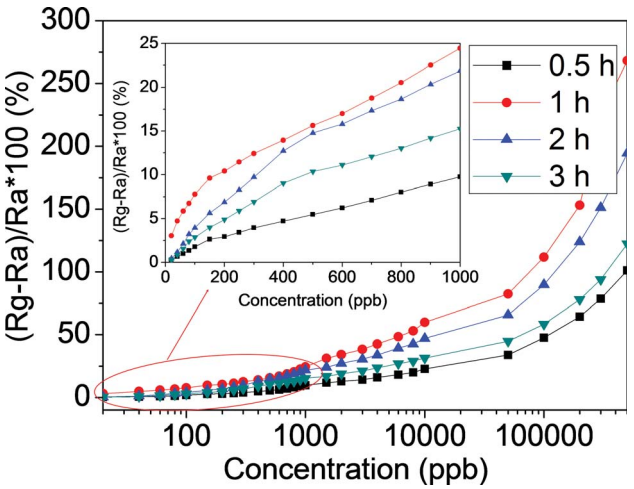

Fig. 5 Relative change of response as a function of NH_3 concentration. The inset shows the response change as a function of NH_3 at low concentration.

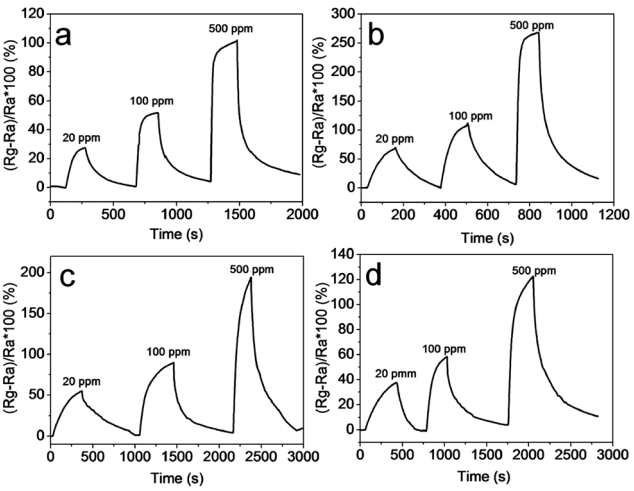

Fig. 6 Response and recovery behavior of SnO_2–PPy hybrid nanofibers with different polymerization times: (a) 0.5 h, (b) 1 h, (c) 2 h, (d) 3 h at 20, 100, and 500 ppm in turn.

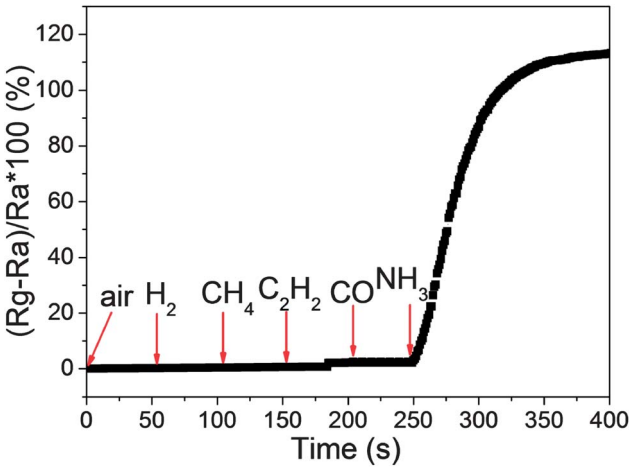

Fig. 7 Anti-interference performance of SnO_2–PPy-1 h with 100 ppm of H_2, CH_4, C_2H_2, CO and NH_3 in turn.

Generally, chemical sensors often have cross-sensitivity, which hinders their practical applications. Herein, anti-interference performance testing was carried out by injecting 100 ppm of H_2, CH_4, C_2H_2, CO and NH_3 into the test chamber in turn, and the results are shown in Fig. 7. It can be seen that the sensor displayed no response until NH_3 was injected. The

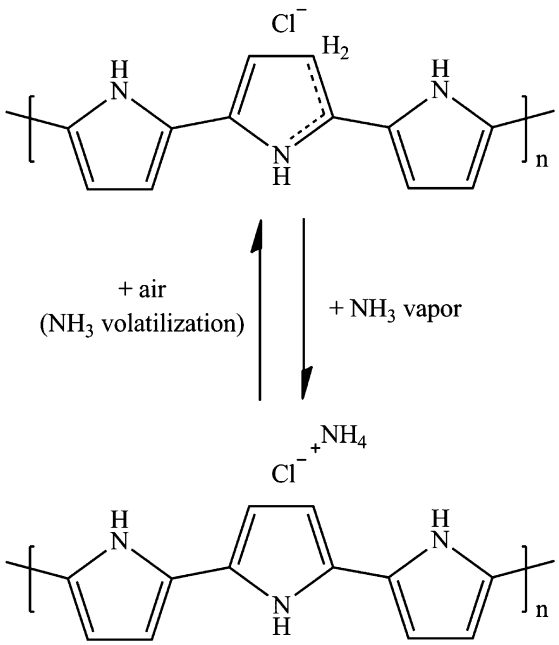

Scheme 1 Interpretation of the sensitivity and reversibility of the PPy–HCl layer.

distinctly different responses to different gases were attributed to the interactions between the sensitive films and the adsorbed gases. When PPy thin sheath interacts with NH_3, the electron transfer between the ammonia molecule and the polymer's positive hole induces a diminution of the sensitive positive charge density which leads to a decrease in the conductance layer. However, the electron donating ability of the other four gases is different from that of NH_3, resulting in the variation in the response characteristics. The whole process can be found in Scheme 1.[56]

3.4 Synergic effect within n-type SnO_2–p-type PPy nano-hybrid-structures during the gas sensing measurement and its verification

In our experiment, the theory of p–n junctions has been introduced into the composite systems to explain the synergic effect and its role in gas detection. It is well known that once p-type semiconductors contact with n-type semiconductors, the holes within the p-type semiconductors will diffuse into the n-type semiconductors and neutralize the free electrons, resulting in positive charges being left within the n-type semiconductors. Likewise, free electrons within the n-type semiconductors diffuse into the p-type semiconductors to neutralize the holes, resulting in negative charges left within the p-type semiconductors. Thus, a space charge region (depleting layer) will form for the equilibrium condition of the p–n junction as shown in Scheme 2.[57,58]

Based on the theory of p–n junctions mentioned above, a novel mechanism involving a synergic effect, within the gas sensing measurement, between the p-type organic (PPy) and n-type inorganic (SnO_2) materials has been established. It is well known that when the outer surface of n-type SnO_2 is coated by p-type PPy as shown in Scheme 3a and b, a p–n junction will form between the interface. Holes within the p-type PPy shell, near the p–n interface, will diffuse into the n-type SnO_2 core to neutralize the free electrons and a new region (region C) will form within the SnO_2 core. Likewise, free electrons within the n-type SnO_2 will diffuse into the PPy shell to neutralize the holes and a new region (region B) will form within the PPy-shell. The formation of regions B and C results in the space charge region (depletion layer) as shown in Scheme 3c. In equilibrium, the space charge region prevents the further diffusion of free electrons and holes from SnO_2 and PPy, respectively. Thus, the whole SnO_2–PPy core–shell nanostructure can be divided into 4 regions, namely, region A, region B, region C and region D.

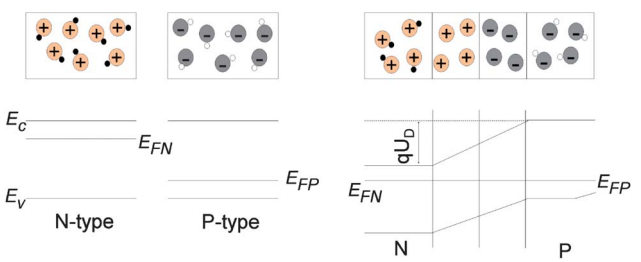

Scheme 2 Schematic diagram of the formation of a p–n junction.

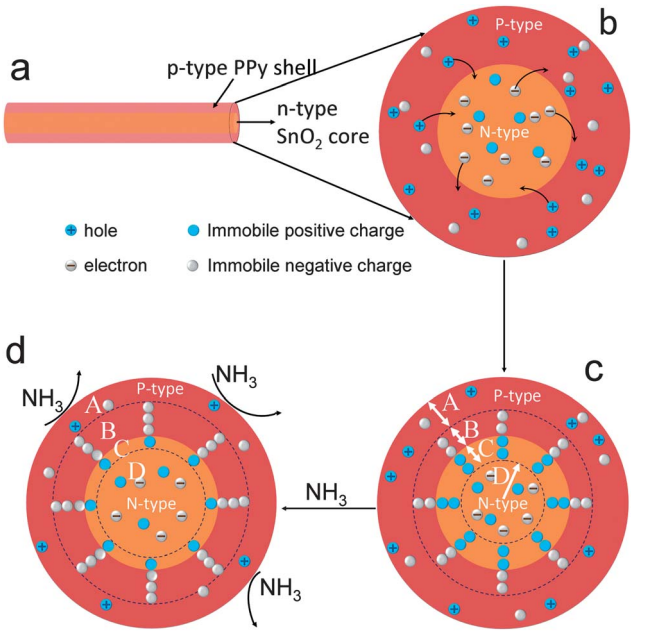

Scheme 3 Schematic diagram of the inter-reaction between 1D n-type SnO_2–p-type PPy core–shell nanofibers and NH_3.

To further prove the formation of the p–n junction, *I–V* tests of SnO_2–PPy composite nanofibers with different vapor polymerization times from 5 min to 3 h were carried out. We can discuss two situations as below:

(1) If a p–n junction does not form between the PPy-shell and the SnO_2-core, the resistance of the SnO_2–PPy composite nanofibers will reduce with increasing polymerization time because the resistance of PPy is much lower than that of SnO_2.

(2) On the contrary, if a p–n junction exists between the PPy-shell and the SnO_2-core, the resistance of the SnO_2–PPy composite nanofibers will firstly increase when the polymerization time is less than 30 min and then reduce when the polymerization time is longer than 30 min. In the former stage, the thickness of PPy is thinner than that of region B (as shown below), thus upon increasing the polymerization time, the thickness of the PPy-shell will increase and more holes from the PPy-shell will enter the SnO_2 to neutralize the free electrons within the SnO_2-core, resulting in the resistance further improving. In the latter stage, the thickness of the PPy-shell is thicker than that of region B, thus upon increasing the polymerization time, the thickness of region A will increase, resulting in the reduction in the resistance.

Fig. 8a and b show the forward bias *I–V* curves on a linear scale and semilog scale, respectively, which match the p–n junction theory. When the polymerization time was short (*e.g.* 5, 10, or 15 min), the resistance of the materials increased as the polymerization time was prolonged. When the polymerization time was long (*e.g.* >30 min), the resistances of our materials mainly depended on the PPy shells (region A), resulting in resistances that are orders of magnitude lower. These data directly prove the formation of the p–n junction.

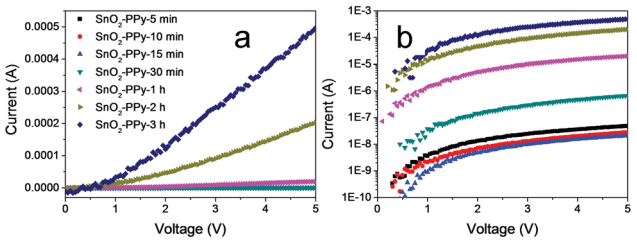

Fig. 8 The forward bias *I–V* curves of the as-prepared composite nanofibers on (a) a linear scale and (b) a semilog scale.

When the materials are exposed to the air, the overall resistance (R) can be represented as follows:

$$\frac{1}{R}=\frac{1}{R_A}+\frac{1}{R_B}+\frac{1}{R_C}+\frac{1}{R_D} \quad (1)$$

Where, R_A, R_B, R_C, and R_D are the resistances of the PPy layer out space charge region, the PPy layer within the space charge region, the SnO_2 layer within the space charge region, and the SnO_2 nanofiber out space charge region, respectively. R_C and R_D within the SnO_2 are much larger than the corresponding values for PPy. The overall resistance (R) can be simplified as:

$$\frac{1}{R}=\frac{1}{R_A}+\frac{1}{R_B} \quad (2)$$

As the samples were exposed to NH_3, both the holes within region A and residual holes within region B will react with NH_3, resulting in a reduction in the hole concentrations within regions A and B, making the resistances R_A and R_B become larger. At this time, the holes within region C will move back to the whole PPy shell to complement the concentration of holes, making the thickness of region C become smaller. Most importantly, for a reduction in the hole concentration within the whole PPy shell, the thickness of region B must further expand, resulting in the resistance R_A being further increased, thus, the response has been further amplified as illustrated in Scheme 3c and d. This amplification effect is the synergic effect within n-type SnO_2–p-type PPy nano-hybrid-structures during gas sensing measurements.

From our theory, it can be found that the thicknesses of the whole PPy layer and region B are critical keys to the sensing performance. Two hyphotheses can be put forward.

(i) *Hypothesis 1*: Situation 1: The whole PPy layer is thinner or equal to the thickness of region B. The overall resistance (R) is dependent on R_B. In this situation, the variation in the response to the target molecules is relatively small due to the lower concentration of residual holes within region B. Thus, upon increasing the thickness of the PPy layer, the concentration of residual holes will increase, resulting in a larger response. Situation 2: The whole PPy layer is thicker than region B. The overall resistance (R) is dependent on R_A and R_B. At this time, both the concentration of residual holes within region B and the expansion of region B within region A can be regarded as fixed. Thus, the response to target molecules is mainly dependent on the thickness of region A. Thus, upon increasing the thickness of region A, the response will become smaller due to the low diffusion rate of the target molecules within the thinner sensing body (as proven in Fig. 5). Additionally, we can also conclude that the response in situation 1 is less than that in situation 2.

(ii) *Hypothesis 2*: The thickness of the whole PPy layer is fixed. The sensing performance can be further tuned by controlling the properties of region B. Situation 3: When the thickness of the whole PPy layer is greater than that of region B, a larger response can be achieved by improving the diffusion rate of the holes and free electrons within the space charge region, and owing to the improved diffusion rate of holes and free electrons the thickness of region B can be increased, resulting in the reduction of region A, namely, the sensing body becomes thinner. Situation 4: If the thickness of the whole PPy layer is thinner than that of region B, a smaller response will be obtained by improving the diffusion rate of the holes and free electrons within the space charge region, and owing to the improved diffusion rate of holes and free electrons this can further lower the concentration of residual holes within region B.

To further verify such p–n heterojunction sensing performance, a series of experiments were carried out. As proven in Fig. 5, it was found that SnO_2–PPy-1 h exhibited the highest response. Meanwhile, the response of SnO_2–PPy-0.5 h exhibited the lowest response. Those results confirm that when the polymerization time was 1 h, the thickness of the PPy layer was thicker than that of region B. So we shortened the

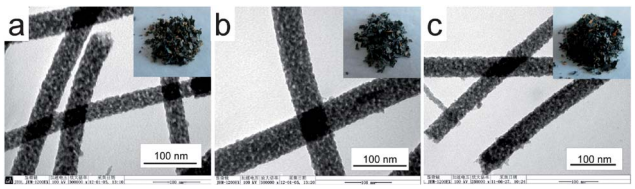

Fig. 9 TEM images of the SnO_2–PPy hybrid nanofibers with different shortened polymerization times: (a) 5 min, (b) 10 min, (c) 15 min. The insets show the optical photographs.

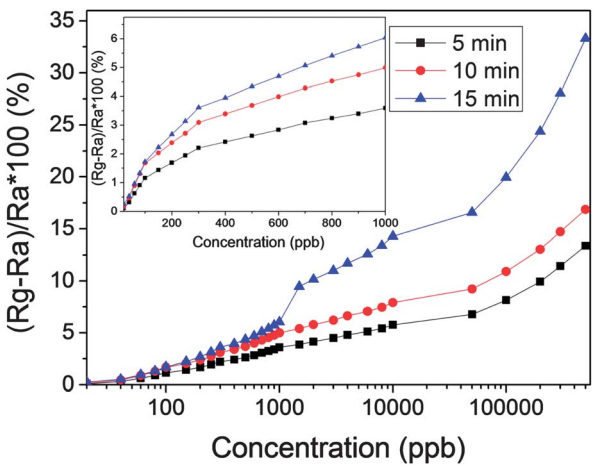

Fig. 10 Response variation *versus* NH_3 concentration of SnO_2–PPy hybrid nanofibers with different shortened polymerization times at room temperature. The inset shows the response to NH_3 at low concentrations.

polymerization time to 15, 10, and 5 min. Fig. 9 presents TEM images of the SnO_2–PPy composite nanofibers with different shortened polymerization times. In comparison with the SnO_2–Fe_2O_3 composite nanofibers (Fig. 1a), the colors of the samples (insets in Fig. 9) changed from brownish yellow to dark, proving the formation of the PPy layer. FT-IR was used to characterize the formation of PPy (Fig. S2†).

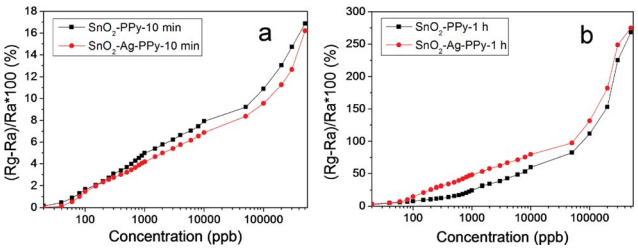

Fig. 11 Comparison of sensing performances of SnO_2–PPy and SnO_2–Ag–PPy composite nanofibers with the same polymerization times: (a) 10 min, (b) 1 h.

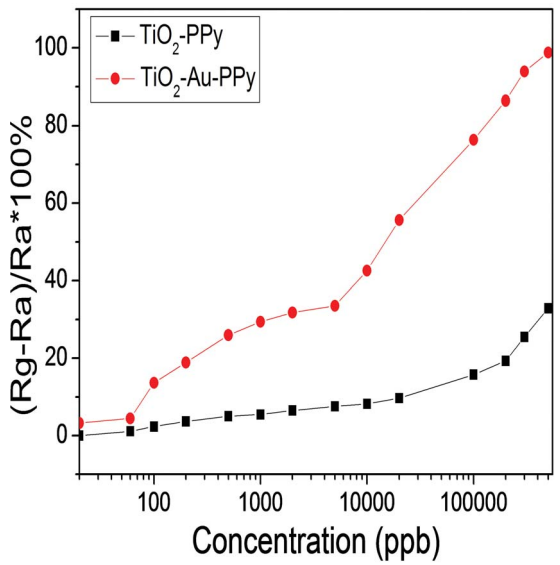

Fig. 12 The NH_3 sensing performances of TiO_2–PPy and TiO_2–Au–PPy core–shell nanofibers.

Fig. 10 shows the response changes of the samples with different concentrations of NH_3 (20 ppb to 500 ppm), with other conditions fixed. From the curves, it can be clearly seen that the response is increased by prolonging the polymerization time; such a result can directly prove that the thickness of the whole PPy layer is thinner than or equal to the thickness of region B. The overall resistance (R) is dependent on R_B. In this situation, upon increasing the thickness of the PPy layer, the concentration of residual holes will increase, resulting in larger response (as mentioned in situation 1 within hypothesis 1). Furthermore, we also find that all the responses of the samples with polymerization times of less than or equal to 30 min are smaller than those of the samples with polymerization times of longer than 1 h as shown in Fig. 5, confirming that the response in situation 1 is less than that in situation 2 (as mentioned in hypothesis 1).

To verify the validity of hypothesis 2, interfacial Ag nanoparticles were introduced into the PPy–SnO_2 composite nanofibers (the morphologies of the SnO_2–Ag–PPy composite nanofibers can be found in Fig. S3†). The existence of metal (Ag or Au) nanoparticles could accelerate the electron transition between the p and n semiconductors due to the modest work function of metal between that of p and n semiconductors (further details can be found in the ESI†), resulting in a thicker region B. The sensing performances of SnO_2–PPy and SnO_2–Ag–PPy were measured and are shown in Fig. 11. When the polymerization time was fixed at 10 min, the SnO_2–PPy composite nanofibers displayed a larger response than that of the SnO_2–Ag–PPy composite nanofibers as shown in Fig. 11a, proving the validity of situation 4 mentioned in hypothesis 2. When the polymerization time was 1 h, the SnO_2–PPy composite nanofibers showed a smaller response than the SnO_2–Ag–PPy composite nanofibers as shown in Fig. 11b, confirming the validity of situation 3 mentioned in hypothesis 2.

3.5 The generality of our theory and its application in fabricating sensitive gas sensors

Both TiO_2–PPy and TiO_2–Au–PPy nano-hybrid-structures with polymerization times of 2 h were prepared to verify the generality of our theory (the morphologies and structural characterizations of the TiO_2–PPy-2 h and TiO_2–Au–PPy-2 h core–shell

Table 1 Comparison of the responses of various PPy based NH_3 sensors

	Concentration						
Materials	0.02 ppm	0.5 ppm	5 ppm	20 ppm	50 ppm	100 ppm	500 ppm
SnO_2–Ag–PPy (in our experiment)	3.15	6.15	68.7	83.2	97.47	131.85	274.7
TiO_2–Au–PPy (in our experiment)	3.2	26	33.5	35.6		76.4	98.9
PPy-coated TiO_2–ZnO (ref. 45)		2	7				34
PPy–$ZnSnO_3$ nanocomposite (ref. 49)				2.5	4.6	6.9	
TiO_2–PPy thin film (ref. 53)					40	55	85
PPy + Pd composite (ref. 54)					13	18	35
PPy nanowire (ref. 59)		1	3.5	5	9	11	
PPy nanowire (ref. 60)					8	12	
PPy–polymethylmethacrylate composite film (ref. 61)				2		3	8

nanofibers can be found in Fig. S3 and S4†). Fig. 12 shows the gas sensing performance. It can be clearly seen that the response of the TiO_2–Au–PPy-2 h nanofibers is much larger than that of the TiO_2–PPy-2 h nanofibers, confirming the generality of our theory. Additionally, the gas sensing performances obtained from our SnO_2 core–shell nanofibers are much better than those of previously reported PPy gas sensors,[45,49,53,54,59–61] as summarized in Table 1, which means that the synergic effect can be used as a powerful tool to fabricate sensitive gas sensors.

4 Conclusions

For the first time, p–n junction theory has been used to elucidate the synergic effect in p–n heterojunction gas sensors. Additionally, the validity and the generality of our hypothesis for the synergic effect have been verified. We believe that our results can construct a powerful platform to better understand and design sensitive gas sensors in the future.

Acknowledgements

This work has been supported by National 973 Project (no. 2007CB936203 and S2009061009), NSF China (no. 50973038 and no. 51003036) and Doctoral Interdisciplinary Sponsored Research Project of Jilin University (no. 2012JC006).

Notes and references

1 S. A. DiBenedetto, A. Facchetti, M. A. Ratner and T. J. Marks, *Adv. Mater.*, 2009, **21**, 1407.
2 Q. Cao, M. G. Xia, M. Shim and J. A. Rogers, *Adv. Funct. Mater.*, 2006, **16**, 2355.
3 J. H. Na, M. Kitamura and Y. Arakawa, *Appl. Phys. Lett.*, 2008, **93**, 213505.
4 A. L. Briseno, T. W. Holcombe, A. I. Boukai, E. C. Garnett, S. W. Shelton, J. J. M. Frechet and P. D. Yang, *Nano Lett.*, 2010, **10**, 334.
5 S. Riad, *Thin Solid Films*, 2000, **370**, 253.
6 K. S. Karimov, M. M. Ahmed, S. A. Moiz and M. I. Fedorov, *Sol. Energy Mater. Sol. Cells*, 2005, **87**, 61.
7 P. L. Ong and I. A. Levitsky, *Energies*, 2010, **3**, 313.
8 Y. B. Guo, Y. J. Zhang, H. B. Liu, S. W. Lai, Y. L. Li, Y. J. Li, W. P. Hu, S. Wang, C. M. Che and D. B. Zhu, *J. Phys. Chem. Lett.*, 2010, **1**, 327.
9 M. Sofos, J. Goldberger, D. A. Stone, J. E. Allen, Q. Ma, D. J. Herman, W. W. Tsai, L. J. Lauhon and S. I. Stupp, *Nat. Mater.*, 2009, **8**, 68.
10 F. Garnier, *J. Opt. A: Pure Appl. Opt.*, 2002, **4**, S247.
11 C. Taussig, S. Moller, S. R. Forrest, C. Perlov and W. Jackson, *J. Appl. Phys.*, 2003, **94**, 7811.
12 S. Smith and S. R. Forrest, *Appl. Phys. Lett.*, 2004, **84**, 5019.
13 G. Luka, T. Krajewski, L. Wachnicki, A. Szczepanik, J. D. Fidelus, A. Szczerbakow, E. Lusakowska, K. Kopalko, E. Guziewicz and M. Godlewski, *Acta Phys. Pol., A*, 2008, **114**, 1229.
14 Y. B. Guo, Q. X. Tang, H. B. Liu, Y. J. Zhang, Y. L. Li, W. P. Hu, S. Wang and D. B. Zhu, *J. Am. Chem. Soc.*, 2008, **130**, 9198.
15 M. M. Ahmed, K. S. Karimov and S. A. Moiz, *IEEE Trans. Electron Devices*, 2004, **51**, 121.
16 F. Yakuphanoglu, *Synth. Met.*, 2007, **157**, 859.
17 B. K. Sharma, N. Khare and S. Ahmad, *Solid State Commun.*, 2009, **149**, 771.
18 T. Gebauer and G. Schmid, *Z. Anorg. Allg. Chem.*, 1999, **625**, 1124.
19 Z. Cao, B. Y. Du, T. Y. Chen, H. T. Li, J. T. Xu and Z. Q. Fan, *Langmuir*, 2008, **24**, 5543.
20 Z. Cao, B. Y. Du, T. Y. Chen, J. J. Nie, J. T. Xu and Z. Q. Fan, *Langmuir*, 2008, **24**, 12771.
21 X. J. Wan, D. Wang and S. Y. Liu, *Langmuir*, 2010, **26**, 15574.
22 H. Li, S. Inoue, K. Machida and G. Adachi, *J. Lumin.*, 2000, **87**, 1069.
23 P. Matyba, K. Maturova, M. Kemerink, N. D. Robinson and L. Edman, *Nat. Mater.*, 2009, **8**, 672.
24 L. Geng, Y. Zhao, X. Huang, S. Wang, S. Zhang and S. Wu, *Sens. Actuators, B*, 2007, **120**, 568.
25 M. K. Ram, O. Yavuz, V. Lahsangah and M. Aldissi, *Sens. Actuators, B*, 2005, **106**, 750.
26 Y. Wu, S. X. Xing and J. C. Fu, *J. Appl. Polym. Sci.*, 2010, **118**, 3351.
27 K. Suri, S. Annapoorni, A. K. Sarkar and R. P. Tandon, *Sens. Actuators, B*, 2002, **81**, 277.
28 L. N. Geng, *Synth. Met.*, 2010, **160**, 1708.
29 M. Kimura, R. Sakai, S. Sato, T. Fukawa, T. Ikehara, R. Maeda and T. Mihara, *Adv. Funct. Mater.*, 2012, **22**, 469.
30 M. Ammam and E. B. Easton, *J. Mater. Chem.*, 2011, **21**, 7886.
31 S. D. Evans, S. R. Johnson, Y. L. Cheng and T. H. Shen, *J. Mater. Chem.*, 2000, **10**, 183.
32 N. J. Pinto, R. Gonzalez, A. T. Johnson and A. G. MacDiarmid, *Appl. Phys. Lett.*, 2006, **89**, 033505.
33 D. Li and Y. N. Xia, *Adv. Mater.*, 2004, **16**, 1151.
34 X. F. Lu, C. Wang and Y. Wei, *Small*, 2009, **5**, 2349.
35 I. S. Chronakis, *J. Mater. Process. Technol.*, 2005, **167**, 283.
36 J. Huang and Q. Wan, *Sensors*, 2009, **9**, 9903.
37 B. Ding, M. R. Wang, J. Y. Yu and G. Sun, *Sensors*, 2009, **9**, 1609.
38 R. Kessick and G. Tepper, *Sens. Actuators, B*, 2006, **117**, 205.
39 Z. Li, H. Zhang, W. Zheng, W. Wang, H. Huang, C. Wang, A. MacDiarmid and Y. Wei, *J. Am. Chem. Soc.*, 2008, **130**, 5036.
40 H. Q. Liu, J. Kameoka, D. A. Czaplewski and H. G. Craighead, *Nano Lett.*, 2004, **4**, 671.
41 S. Virji, J. X. Huang, R. B. Kaner and B. H. Weiller, *Nano Lett.*, 2004, **4**, 491.
42 E. Comini, C. Baratto, G. Faglia, M. Ferroni, A. Vomiero and G. Sberveglieri, *Prog. Mater. Sci.*, 2009, **54**, 1.
43 Z. W. Pan, Z. R. Dai and Z. L. Wang, *Science*, 2001, **291**, 1947.
44 W. Jin, W. Chen, Y. Lu, C. X. Zhao and Y. Dai, *2010 3rd International Nanoelectronics Conference* 2010, vol. 1, p. 431.
45 Y. Wang, W. Z. Jia, T. Strout, A. Schempf, H. Zhang, B. K. Li, J. H. Cui and Y. Lei, *Electroanalysis*, 2009, **21**, 1432.
46 Z. X. Wang and L. Liu, *Mater. Lett.*, 2009, **63**, 917.
47 A. O. Porto, J. M. Pernaut, H. Daniel, P. J. Schilling and M. C. M. Alves, *Synth. Met.*, 1999, **104**, 89.

48 A. Bhattacharya and A. De, *Prog. Solid State Chem.*, 1996, **24**, 141.
49 P. Song, Q. Wang and Z. X. Yang, *Mater. Lett.*, 2011, **65**, 430.
50 H. L. Tai, Y. D. Jiang, G. Z. Xie and M. J. Zhao, *Int. J. Inorg. Mater.*, 2007, **22**, 524.
51 L. N. Geng, Y. Q. Zhao, X. L. Huang, S. R. Wang, S. M. Zhang, W. P. Huang and S. H. Wu, *Synth. Met.*, 2006, **156**, 1078.
52 L. N. Geng, S. R. Wang, P. Li, Y. Q. Zhao, S. M. Zhang and S. H. Wu, *Chin. J. Inorg. Chem.*, 2005, **21**, 977.
53 H. L. Tai, Y. D. Jiang, G. Z. Xie, J. S. Yu and M. J. Zhao, *Int. J. Environ. Anal. Chem.*, 2007, **87**, 539.
54 L. J. Hong, Y. Li and M. J. Yang, *Sens. Actuators, B*, 2010, **145**, 25.
55 G. Gustafsson, I. Lundström, B. Liedberg, C. R. Wu, O. Inganäs and O. Wennerström, *Synth. Met.*, 1989, **31**, 163.
56 S. Carquigny, J. Sanchez, F. Berger, B. Lakard and F. Lallemand, *Talanta*, 2009, **78**, 199.
57 W. Shockley, *Bell Syst. Tech. J.*, 1949, **28**, 435.
58 W. Shockley, M. Sparks and G. K. Teal, *Phys. Rev.*, 1951, **83**, 151.
59 D. Kim and B. Y. Yoo, *Sens. Actuators, B*, 2011, **160**, 1168.
60 S. C. Hernandez, D. Chaudhuri, W. Chen, N. V. Myung and A. Mulchandani, *Electroanalysis*, 2007, **19**, 2125.
61 G. Y. Han and G. Q. Shi, *Thin Solid Films*, 2007, **515**, 6986.
62 X. F. Lu, H. Mao and W. J. Zhang, *Nanotechnology*, 2007, **18**, 025604.